

The excitation of spiral density waves through turbulent fluctuations in accretion discs II: Numerical Simulations with MRI driven turbulence

T. Heinemann¹ and J. C. B. Papaloizou¹

¹ *University of Cambridge, Wilberforce Road, Cambridge CB3 0WA*

7 November 2018

ABSTRACT

We present fully three-dimensional local simulations of compressible MRI turbulence with the object of studying and elucidating the excitation of the non-axisymmetric spiral density waves that are observed to always be present in such simulations. They are potentially important for affecting protoplanetary migration through the action of associated stochastic gravitational forces and producing residual transport in MHD inactive regions through which they may propagate. The simulations we perform are with zero net flux and produce mean activity levels corresponding to the Shakura & Sunyaev $\alpha \sim 5 \times 10^{-3}$, being at the lower end of the range usually considered in accretion disc modelling. We reveal the nature of the mechanism responsible for the excitation of these waves by determining the time dependent evolution of the Fourier transforms of the participating state variables. The dominant waves are found to have no vertical structure and to be excited during periodically repeating swings in which they change from leading to trailing. The initial phase of the evolution of such a swing is found to be in excellent agreement with that expected from the WKBJ theory developed in a preceding paper by Heinemann & Papaloizou. However, shortly after the attainment of the expected maximum wave amplitude, the waves begin to be damped on account of the formation of weak shocks. As expected from the theory the waves are seen to shorten in radial wavelength as they propagate. This feature enables nonlinear dissipation to continue in spite of amplitude decrease. As a consequence the waves are almost always seen to be in the non linear regime.

We demonstrate that the important source terms causing excitation of the waves are related to a quantity that reduces to the potential vorticity for small perturbations from the background state with no vertical dependence. We find that the root mean square density fluctuations associated with the waves are positively correlated with both this quantity and the general level of hydromagnetic turbulence. The mean angular momentum transport associated with spiral density waves generated in our simulations is estimated to be a significant fraction of that associated with the turbulent Reynolds stress.

Key words: accretion, accretion discs – turbulence – waves

1 INTRODUCTION

This is the second of two papers which study the excitation of spiral density (SD) waves in accretion discs occurring through the action of stochastic forcing due to turbulence. In practice this has been taken to arise from the magneto-rotational instability (MRI) but excitation resulting from stochastic forcing produced by other mechanisms is expected to lead to similar results. In the preceding paper (Heinemann & Papaloizou 2009, paper I) we developed a WKBJ theory of the excitation process. In this paper we study the wave excitation process directly as it is manifested

in fully nonlinear three dimensional numerical simulations, with the object of elucidating it further and comparing the results with the predictions of the WKBJ theory developed in paper I.

The outline of this paper is as follows. In Section 2 we give a brief review of the shearing box model, the basic equations solved in the simulation, as well as the equations governing the dynamics of SD waves. We also describe the procedure for performing the Fourier transforms of the state variables participating in the excited waves in shearing coordinates. This allows us to identify and then follow the

evolution of wave amplitudes in order to make a detailed comparison with the WKB theory presented in paper I.

In Section 3, after briefly describing the simulation set up and the numerical method used, we present a fully three-dimensional simulation of compressible MRI turbulence in which we directly observe the excitation of large scale, non-axisymmetric SD waves. We discuss their main characteristics and the correlation of the root mean square density fluctuations associated with them with the level of turbulent activity. We go on to study the source terms driving the wave excitation and motivate the simplifying assumption that those proportional to a quantity that is related to the potential vorticity dominate. This assumption enabled us to derive the linear theory of wave excitation presented in paper I. A detailed comparison between this linear theory and simulation outcomes is presented in Section 4. There we follow the time dependent evolution of the appropriate Fourier amplitudes through a swing cycle, during which the wave excitation occurs, in detail. We obtain very good agreement with predictions from the theory developed in paper I. Finally, we discuss and summarize our results in Section 5, indicating the magnitude and the scaling of the wave angular momentum flux with the Reynolds stress and also the wavelength in the azimuthal direction for which the wave excitation phenomenon is optimal.

2 PRELIMINARIES

2.1 The shearing box model

As in paper I we consider an isothermal conducting gas in the shearing box approximation in the absence of vertical stratification. The Cartesian coordinate system (x, y, z) is such that x corresponds to radius, y to azimuth, and z denotes the vertical direction. The equations of motions consist of the continuity equation

$$\mathcal{D}\rho + \nabla \cdot \mathbf{p} = 0, \quad (1)$$

the momentum equation

$$\mathcal{D}\mathbf{p} = -c^2 \nabla \rho - 2\mathbf{\Omega} \times \mathbf{p} + q\Omega \rho_x \mathbf{e}_y + \nabla \cdot \mathbf{T} + \nabla \cdot (2\rho\nu\mathbf{S}) \quad (2)$$

and the induction equation

$$\mathcal{D}\mathbf{B} = \nabla \times (\mathbf{u} \times \mathbf{B} - \eta \nabla \times \mathbf{B}) - q\Omega B_x \mathbf{e}_y \quad (3)$$

where the differential operator

$$\mathcal{D} = \partial_t - q\Omega x \partial_y, \quad (4)$$

accounts for advection by the linear shear $-q\Omega x \mathbf{e}_y$, $\mathbf{\Omega} = \Omega \mathbf{e}_z$ is the angular velocity, ρ is the density, the linear momentum density $\mathbf{p} = \rho \mathbf{u}$ defined in terms of the velocity deviations $\mathbf{u} = (u_x, u_y, u_z)$ from the mean shear, $c = H\Omega$ is the isothermal sound speed, H is the nominal density scale height, the magnetic field $\mathbf{B} = (B_x, B_y, B_z)$ is normalised by the square root of the vacuum permeability μ_0 , in which case the nonlinear stress tensor \mathbf{T} has components

$$T_{ij} = B_i B_j - \delta_{ij} B^2/2 - \rho u_i u_j. \quad (5)$$

\mathbf{S} is the traceless rate-of-strain tensor whose components are given by

$$S_{ij} = \frac{1}{2} \left(\frac{\partial u_i}{\partial x_j} + \frac{\partial u_j}{\partial x_i} - \frac{2}{3} \delta_{ij} \nabla \cdot \mathbf{u} \right) - \frac{q\Omega}{2} (\delta_{ix} \delta_{jy} + \delta_{iy} \delta_{jx})$$

which are seen to include terms arising due to the linear shear. The kinematic viscosity is ν and the resistivity is η .

We consider the governing equations (1–3) to be subject to ‘shearing periodic’ periodic boundary conditions, i.e.

$$f(x + L_x, y - q\Omega t L_x, z, t) = f(x, y, z, t), \quad (6a)$$

$$f(x, y + L_y, z, t) = f(x, y, z, t) \quad (6b)$$

and

$$f(x, y, z + L_z, t) = f(x, y, z, t). \quad (6c)$$

From (6) we see that the domain becomes fully periodic once every shearing time

$$\delta T_s = \frac{L_y/L_x}{q\Omega}. \quad (7)$$

2.2 Wave equations

We developed equations governing the excitation of SD waves in the inviscid limit in paper I. These follow directly from equations (1) and (2). As we will demonstrate, SD waves in the unstratified shearing box exhibit little dependence on the vertical coordinate z so that we may consider vertically averaged quantities (indicated by being contained within angle brackets $\langle \cdot \rangle_z$) for which the wave equations read

$$(\mathcal{D}^2 - c^2 \nabla^2 + \kappa^2) \langle \rho \rangle_z + 2q\Omega \partial_y \langle p_x \rangle_z = -2\Omega \langle \zeta \rangle_z - \partial_x \langle \mathfrak{N}_x \rangle_z - \partial_y \langle \mathfrak{N}_y \rangle_z, \quad (8a)$$

$$(\mathcal{D}^2 - c^2 \nabla^2 + \kappa^2) \langle p_x \rangle_z + 2q\Omega c^2 \partial_y \langle \rho \rangle_z = c^2 \partial_y \langle \zeta \rangle_z + 2\Omega \langle \mathfrak{N}_y \rangle_z + \mathcal{D} \langle \mathfrak{N}_x \rangle_z, \quad (8b)$$

and

$$(\mathcal{D}^2 - c^2 \nabla^2 + \kappa^2) \langle p_y \rangle_z = -c^2 \partial_x \langle \zeta \rangle_z + (q - 2)\Omega \langle \mathfrak{N}_x \rangle_z + \mathcal{D} \langle \mathfrak{N}_y \rangle_z. \quad (8c)$$

Here, $\kappa^2 = 2(2 - q)\Omega^2$ is the square of the epicyclic frequency and we have introduced the divergence of the nonlinear stress tensor $\mathfrak{N} = \nabla \cdot \mathbf{T}$ as a short-hand to denote the nonlinear source terms.

In paper I we postulated that as far as wave excitation is concerned the dominant source term in each of the three wave equations is the linear one appearing first on the right hand sides of (8) and involving the quantity

$$\langle \zeta \rangle_z = \partial_x \langle p_y \rangle_z - \partial_y \langle p_x \rangle_z + (q - 2)\Omega \langle \rho \rangle_z \quad (9)$$

which we refer to as pseudo potential vorticity (or PPV for short). An important property of PPV is that apart from advection by the linear shear, it varies in time due to nonlinear stresses only,

$$\mathcal{D} \langle \zeta \rangle_z = \partial_x \langle \mathfrak{N}_y \rangle_z - \partial_y \langle \mathfrak{N}_x \rangle_z, \quad (10)$$

and is thus conserved for a linear SD wave. Note also that in this limit the change in PPV is equal to the change of potential vorticity, the difference being at most second order in the wave amplitude.

2.3 Decomposition into shearing waves

In the periodic shearing sheet a suitable Fourier basis is given by plane waves with, in the coordinate system adopted, time dependent radial wave numbers. The expansion of any (vertically averaged) fluid variable f in this basis reads

$$\langle f \rangle_z(x, y, t) = \sum_{n_x, n_y} \hat{f}(t) \exp[ik_x(t)x + ik_y y], \quad (11)$$

where \hat{f} is a complex valued wave amplitude and where the wave numbers

$$k_x(t) = \left(\frac{2\pi n_x}{L_x} \right) + q\Omega t \left(\frac{2\pi n_y}{L_y} \right) \quad \text{and} \quad k_y = \frac{2\pi n_y}{L_y}.$$

Each of these so-called shearing waves (Thomson 1887) is uniquely labelled by the pair of integral numbers $n_x, n_y \in \mathbb{Z}$. The radial wave numbers depend linearly on time such that

$$\frac{dk_x}{dt} = q\Omega k_y,$$

which is a consequence of advection by the linear background shear.

Because $k_x(t)/k_y$ increases monotonically if $q\Omega > 0$, every shearing wave evolves from being leading, i.e. $k_x(t)/k_y < 0$, to being trailing, i.e. $k_x(t)/k_y > 0$, as time progresses from $t = -\infty$ to $t = \infty$. The change from leading to trailing is referred to as ‘swing’ and occurs at

$$t_s = -\frac{n_x}{n_y} \delta T_s \quad (12)$$

From linear theory we expect wave excitation to occur at the time of the swing. From (12) we see that different shearing waves swing from leading to trailing at different times so that the excitation process consists of a series of swings that are separated, for a given k_y , by the fixed time interval $\delta t_s = \delta T_s / n_y$.

Expanded in the Fourier basis (11), the SD wave equations (8) for a single shearing wave read

$$\begin{aligned} \frac{d^2 \hat{\rho}}{dt^2} + [\mathbf{k}^2(t)c^2 + \kappa^2] \hat{\rho} + 2q\Omega i k_y \hat{p}_x = \\ - 2\Omega \hat{\zeta} - i k_x(t) \hat{\eta}_x - i k_y \hat{\eta}_y, \end{aligned} \quad (13a)$$

$$\begin{aligned} \frac{d^2 \hat{p}_x}{dt^2} + [\mathbf{k}^2(t)c^2 + \kappa^2] \hat{p}_x + 2q\Omega c^2 i k_y \hat{\rho} = \\ c^2 i k_y \hat{\zeta} + 2\Omega \hat{\eta}_y + \frac{d\hat{\eta}_x}{dt}, \end{aligned} \quad (13b)$$

and

$$\begin{aligned} \frac{d^2 \hat{p}_y}{dt^2} + [\mathbf{k}^2(t)c^2 + \kappa^2] \hat{p}_y = \\ - c^2 i k_x \hat{\zeta} + (q - 2)\Omega \hat{\eta}_x + \frac{d\hat{\eta}_y}{dt}. \end{aligned} \quad (13c)$$

3 SIMULATIONS

The steady state solution for the non-stratified shearing box, for which the density is uniform and the velocity takes the form of a linear shear, is subject to the magneto-rotational instability when a relatively weak magnetic field with zero

net flux is introduced. This ultimately results in the production of turbulence that is powered by the linear shear and attains a statistically steady state (Hawley et al. 1995; Brandenburg et al. 1995; Stone et al. 1996).

We have carried out local, three-dimensional simulations of accretion disk turbulence induced by the MRI. The purpose of these simulations is threefold. Firstly to study and quantify the mode of excitation of SD waves in a turbulent shearing box, secondly to justify some of the simplifying assumptions that were made in order to proceed with the theoretical analysis of the excitation mechanism given in paper I, and thirdly to provide results which can be tested against predictions made from this theory (see Section 4) so that the nature of the phenomenon and the implied dependence on physical parameters can be confirmed.

3.1 Setup

We use the Pencil Code (see e.g. Brandenburg & Dobler 2002) to solve the MHD equations in the shearing box. The numerical method relies on using sixth-order central finite differences for the evaluation of spatial derivatives and a third-order Runge-Kutta scheme for time integration. The method is stabilized by imposing explicit diffusion coefficients in all evolution equations. The shearing box boundary conditions are implemented via sixth-order polynomial interpolation. The code solves the isothermal MHD equations in the shearing box approximation (1–3) in terms of mass density ρ , fluid velocity \mathbf{u} , and, to ensure that $\nabla \cdot \mathbf{B} = 0$, the induction equation is rewritten in terms of the magnetic vector potential \mathbf{A} with $\mathbf{B} = \nabla \times \mathbf{A}$. Details are given in Appendix A.

The setup is similar to the one used for a code comparison in Fromang et al. (2007). We choose a box size of $(L_x, L_y, L_z) = (H, 4H, H)$ and a resolution of $(N_x, N_y, N_z) = (128, 512, 128)$. Fromang et al. (2007) showed that in the zero-net-flux case, the level of MRI turbulence critically depends on the magnetic Prandtl number $\text{Pm} = \nu/\eta$, i.e. the ratio of kinematic viscosity to magnetic resistivity. Here we set $\nu = 32 \cdot 10^{-5} H^2 \Omega$ and $\eta = 8 \cdot 10^{-5} H^2 \Omega$ such that $\text{Pm} = 4$. In this case we observe MRI turbulence that is, as in Fromang et al. (2007), sustained for several hundred orbits and expected to be numerically resolved for the values of the diffusion coefficients that we impose.

3.2 Volume averages

In Fig. 1 we plot the root mean squared velocity and density fluctuations, calculated as volume averages over the box, and volume averages of the Reynolds and Maxwell stress as functions of time. The initial peak that is seen in the velocity fluctuations and in the Reynolds and Maxwell stresses is due to exponential growth of axisymmetric MRI modes. After roughly 4 Orbits, this so-called channel solution is torn apart by secondary, non-axisymmetric instabilities (see e.g. Latter et al. 2009 and references therein) and the system enters a quasi steady state of sustained MRI turbulence.

The velocity fluctuations in this state are an order of magnitude less in amplitude than the speed of sound. In spite of the strongly subsonic nature of the turbulence we observe density fluctuations with a temporal mean of about

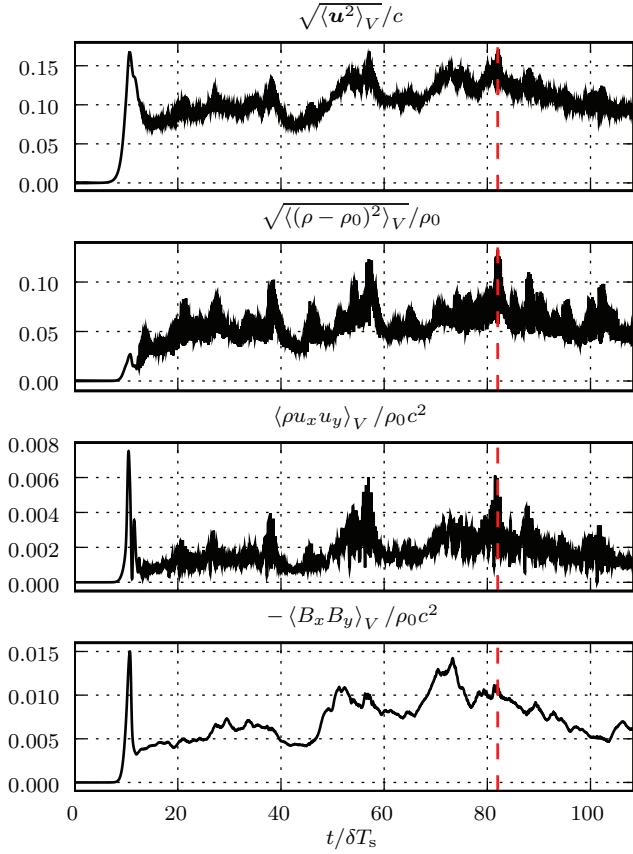


Figure 1. Temporal evolution of root mean squared velocity and density fluctuations (upper two panels) and of the volume averaged Reynolds and Maxwell stress (lower two panels). The red dashed line corresponds to $t = 82 \delta T_s$ at which point the largest density fluctuation occurs.

6 per cent and peak values of more than 15 per cent of the background value. We will see that the peak density fluctuations are due to high-frequency, non-axisymmetric SD waves that are excited via the mechanism discussed in paper I. Because these waves are trailing, they lead to outward angular momentum transport. This manifests itself in a strong correlation between the density fluctuations and the mean Reynolds stress. At *peak* values, the Reynolds stress may even become comparable to the Maxwell stress although we note that the former fluctuates rapidly in time so that the net angular momentum transport due to SD waves is less significant than it may appear at first glance. We will attempt to quantify the amount of angular momentum transport due to SD waves later in this paper.

We note that the Maxwell stress fluctuates in time much less rapidly than, and is only very weakly correlated with, the other (purely hydrodynamic) quantities. This is because SD waves are non-magnetic and the Maxwell stress varies on a time scale comparable to the turn over time scale of the turbulence which in this case is much longer than the inverse SD wave frequency.

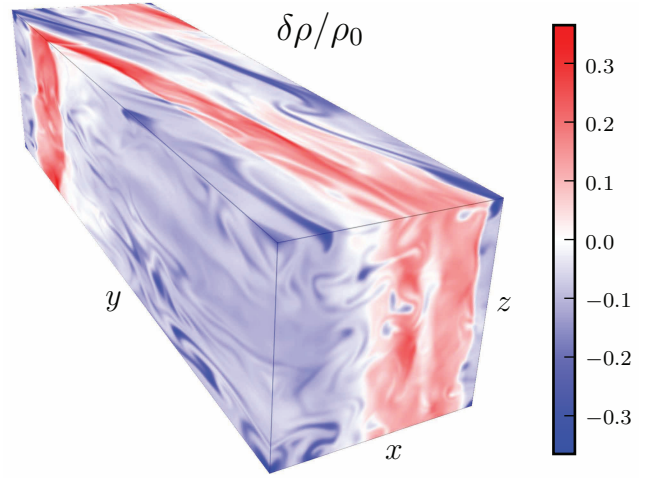


Figure 2. Pseudo-colour image of mass density on the faces of the computational domain. This snapshot is taken at $t = 82 \delta T_s$ where we observe the largest peak in the volume averaged density fluctuations shown in Fig. 1.

3.3 Flow structure in real space

The typical large scale three-dimensional structure of the turbulent flow is depicted in Fig. 2 where we show the mass density field projected onto the faces of the computational domain¹. This snapshot is taken at $t = 82 \delta T_s$ where we observe the largest peak in the volume averaged density fluctuations shown in Fig. 1.

The wave crests are seen to propagate at an inclined angle within the horizontal xy -plane and display little dependence on z . In order to ease the subsequent analysis, as in paper I, we may thus integrate over z and will look at vertically averaged quantities only from now on.

In Fig. 3 we plot false colour images of such vertical averages at the same instance in time as shown in Fig. 2. Large scale wave crests are clearly visible in $\langle \rho \rangle_z$, $\langle p_x \rangle_z$ and, to a lesser extent, in $\langle p_y \rangle_z$. The waves are trailing and always occur in pairs where one wave propagates in a direction opposite to the other wave. That this has to be the case is clear from symmetry considerations of the shearing sheet and we recall that our linear theory predicts pairwise excitation of waves with equal amplitude but oppositely directed wave vectors.

In contrast to $\langle \rho \rangle_z$, $\langle p_x \rangle_z$, and $\langle p_y \rangle_z$, the pseudo potential vorticity

$$\langle \zeta \rangle_z = \partial_x \langle p_y \rangle_z - \partial_y \langle p_x \rangle_z + (q - 2)\Omega \langle \rho \rangle_z$$

does not display a corresponding large scale wave structure but instead consists of smaller scale turbulent structures that are, as is characteristic for accretion disc turbulence, elongated in the shearwise direction. The absence of large scale wave structure in $\langle \zeta \rangle_z$ is reminiscent of the fact that $\langle \zeta \rangle_z$ is conserved for a linear wave, see (10), and the justification for why we are allowed to treat $\langle \zeta \rangle_z$ as a source term for wave excitation, as was done in paper I, in the first place.

¹ An animated version of Fig. 2 and Fig. 3 below is provided as part of the on-line supplements to this article

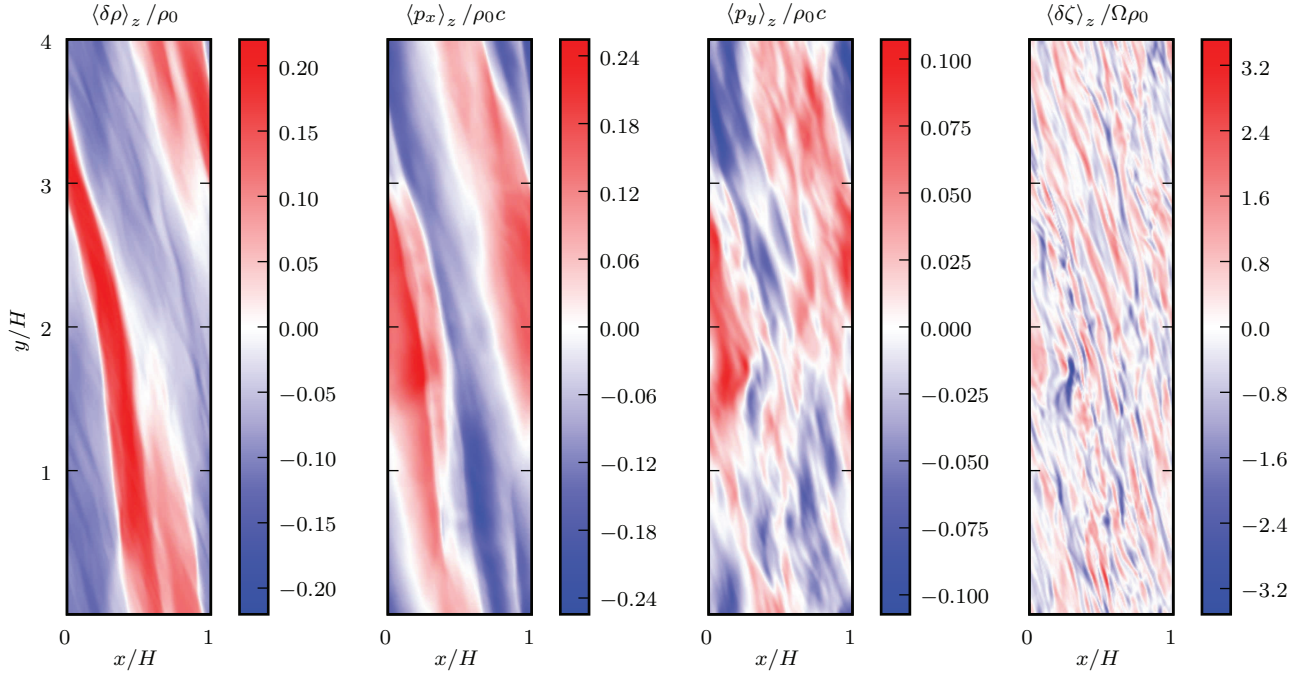


Figure 3. Pseudo colour images of z -averaged quantities at the same instance in time as in Fig. 2. Non-axisymmetric waves are clearly visible in $\langle \rho \rangle_z$ and $\langle p_x \rangle_z$, and to a lesser extent in $\langle p_y \rangle_z$. There will be a system of regularly repeating wave crests when boxes are stacked together to fill space by application of the periodicity conditions. In contrast to this, the waves are not visible in $\langle \delta \zeta \rangle_z$, where $\delta \zeta = \zeta - \zeta_0$ is the PPV deviation from the constant background value $\zeta_0 = (q - 2)\Omega\rho_0$.

3.4 Evolution of single shearing wave

A more revealing picture of the evolution of SD waves as observed during the simulation may be obtained in Fourier space. For this purpose we will look at the discrete Fourier transform (DFT) of vertically averaged quantities as shown in Fig. 3. Taking a two-dimensional spatial DFT in the shearing sheet is non-trivial due to the presence of the linear background shear and requires a coordinate transformation to shearing coordinates, see Appendix B. This coordinate transformation can be done very conveniently by first taking the DFT along the periodic y -direction, then applying an x -dependent phase shift to achieve full periodicity in x , and finally taking the DFT along the x -direction. Further details are given in the Appendix B. This procedure allows us to uniquely assign a time-dependent radial wave number $k_x(t)$ as well as a (constant) azimuthal wave number k_y to a given Fourier amplitude obtained from the DFT, enabling us to follow individual plane waves as they swing from leading to trailing during the course of the simulation.

In Fig. 4 we plot the evolution of the wave amplitudes of the $\hat{\rho}$, \hat{p}_x , and \hat{p}_y for a single shearing wave with azimuthal wave number $k_y = 2\pi/L_y$. Excitation occurs when the wave swings from leading to trailing, i.e. when $k_x(t) \approx 0$, which for this particular wave happens at $t = 81\delta T_s$. The maximum density amplitude of $\text{Re } \hat{\rho} \approx 0.08\rho_0$ is obtained when $k_x(t) \approx 2\pi/H$ or, equivalently, around $t = 82\delta T_s$, i.e. roughly one shearing time later. In Fig. 4 we are thus looking at the Fourier representation of the wave seen in Fig. 2 and Fig. 3 and thus at that particular wave responsible for the large peak in the volume averaged density fluctuations indicated by the dashed red line in Fig. 1.

We note that the wave undergoes significant damping for $k_x(t)H \gtrsim 2\pi$. This decay is in stark contrast to linear theory which either predicts an *algebraic* decrease (for \hat{p}_y) or even increase (for $\hat{\rho}$ and \hat{p}_x) of the wave amplitude with time (see paper I) and therefore needs to be attributed to nonlinear effects. We will comment on this further in Section 4.

The simulation allows us not only to monitor the wave amplitudes $\hat{\rho}$, \hat{p}_x , and \hat{p}_y for a single shearing wave as it evolves in time, but also the various source terms occurring on the right sides of the SD wave equations (13), and to assess the relative importance of these terms for wave excitation.

There are both linear source terms involving the pseudo potential vorticity as well as nonlinear terms involving the vector $\hat{\mathfrak{T}} = i\mathbf{k} \cdot \hat{\mathbf{T}}$, where \hat{T}_{ij} is the Fourier transform of the nonlinear stress tensor (5).

In Fig. 5 we plot the Fourier amplitudes of $\hat{\zeta}$ and the \hat{T}_{ij} for the wave shown in Fig. 4. We see that $\hat{\zeta}$ is – compared to the $\hat{\rho}$, \hat{p}_x , \hat{p}_y , and the nonlinear stresses \hat{T}_{ij} – a slowly varying function of time. When wave excitation occurs around $k_x(t) = 0$ there is no sign of oscillating behaviour in $\hat{\zeta}$. This is a manifestation of PPV conservation to linear order, see (10).

Furthermore, at the time of wave excitation, the amplitude of $\hat{\zeta}$ is more than an order of magnitude larger than the amplitude of any of the components of the nonlinear stress tensor \hat{T}_{ij} suggesting, as these quantities measure their relative contributions to the source terms in equations (13), that it is indeed the pseudo potential vorticity, and thus the linear source term, that is primarily responsible for wave

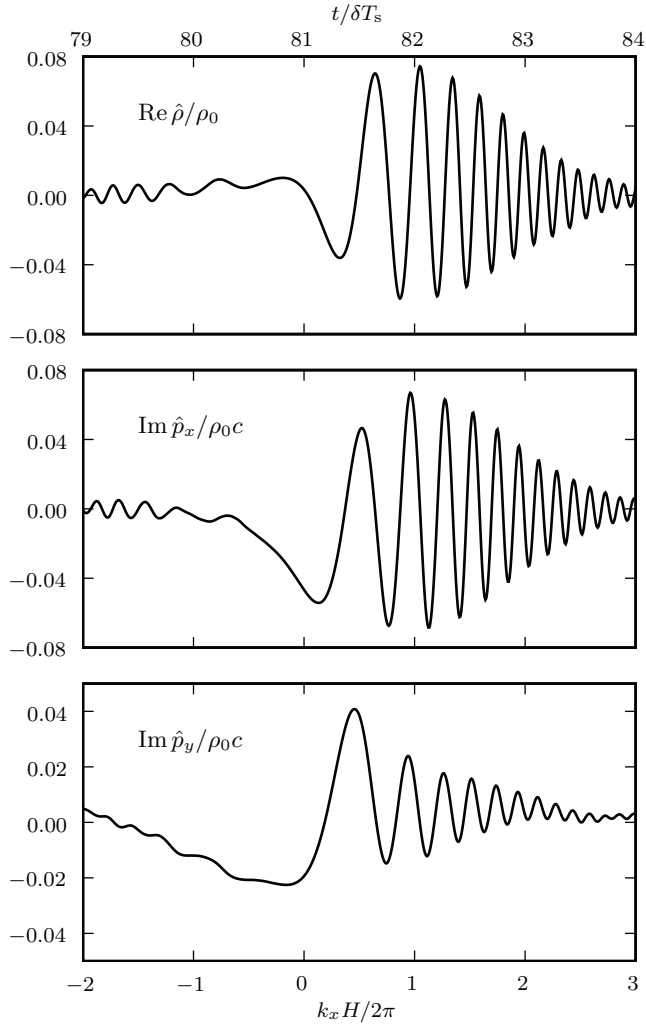


Figure 4. Fourier amplitudes of density and linear momenta for a single shearing wave with azimuthal wave number $k_y = 2\pi/L_y$ as it swings from leading to trailing. Excitation occurs when $k_x(t) = 0$ or, equivalently, at $t = 81 \delta T_s$. This is thus the same wave that is shown in Fig. 2 and Fig. 3.

excitation. We will provide more evidence for this claim in Section 4.

4 COMPARISONS WITH ASYMPTOTIC THEORY

The evolution of SD waves in the shearing sheet is described mathematically by the time-dependent forced oscillator equations (13). Wave excitation is due to the presence of inhomogeneous source terms in these equations and is found – as demonstrated in the preceding section – to occur at the swing stage, i.e. when the time dependent radial wave number $k_x(t) = 0$.

In paper I we derived analytic solutions to the governing equations (13) that are able to capture this swing excitation. These solutions are asymptotic in the parameter

$$\epsilon = \frac{q\Omega k_y c}{k_y^2 c^2 + \kappa^2},$$

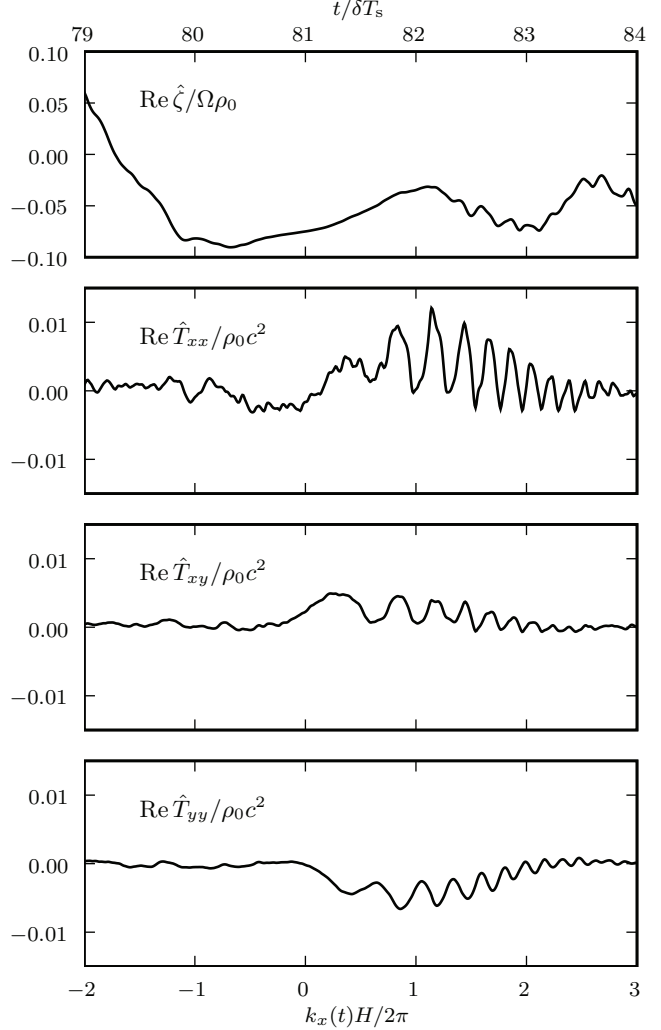


Figure 5. Fourier amplitudes of the pseudo potential vorticity and the components of the nonlinear stress tensor. All of these appear as sources on the right hand side of the SD wave-equations (8).

which is small in both the low and the high azimuthal wave number limit, given by $k_y c \ll \kappa$ and $k_y c \gg \kappa$, respectively. The asymptotic solutions can be written as the sum of a non-oscillatory, vortical solution – called the balanced solution – to the inhomogeneous problem, and standard WKB solutions to the free wave equations that contain the oscillatory part of the solutions and describe the excited SD waves.

A key hypothesis in our analysis in paper I was that the dominant source term for wave excitation is the linear term involving the pseudo potential vorticity $\hat{\zeta}$ and that nonlinear stresses contribute to the excitation only indirectly by generating $\hat{\zeta}$ prior to the swing via (10). This assumption renders the analysis as essentially linear. We have shown in Section 3.4 that the pseudo potential vorticity for a large amplitude SD wave observed in the simulation is more than an order of magnitude greater in size than the nonlinear stresses when the excitation occurs. This suggests that our quasi-linear description of the excitation process is indeed valid and we are now in a position to verify this assertion

by comparing the observed wave amplitudes with our predictions from linear theory.

Expressed in dimensional form, the leading order balanced solutions for $\hat{\rho}$, \hat{p}_x , and \hat{p}_y can be obtained from the relations given in paper I as

$$\bar{\rho} = \hat{\zeta} \operatorname{Re} \left(\frac{ik_y c - 2\Omega}{k^2 c^2 + \kappa^2 + 2q\Omega ik_y c} \right), \quad (14a)$$

$$\bar{p}_x = i\hat{\zeta} c \operatorname{Im} \left(\frac{ik_y c - 2\Omega}{k^2 c^2 + \kappa^2 + 2q\Omega ik_y c} \right), \quad (14b)$$

$$\bar{p}_y = i\hat{\zeta} c \operatorname{Re} \left(\frac{ik_x c}{k^2 c^2 + \kappa^2} \right), \quad (14c)$$

where the SD wave frequencies

$$\omega = \sqrt{k^2 c^2 + \kappa^2} \quad \text{and} \quad \omega_+ = \sqrt{\omega^2 + 2q\Omega ik_y c}.$$

Note that these solutions include the full time dependence of the source.

We are, however, mainly interested in the oscillatory wave part of the solutions, i.e. the WKBJ solutions to the homogeneous problem given in paper I, which may be written as

$$\tilde{\rho} = -\zeta_s \Omega^{-1} \operatorname{Im} \left[\mathcal{A}_+ \sqrt{\Omega/\omega_+} \sin \left(\int_0^t \omega_+ dt' \right) \right] \quad (15a)$$

and

$$\tilde{p}_x = i\zeta_s H \operatorname{Re} \left[\mathcal{A}_+ \sqrt{\Omega/\omega_+} \sin \left(\int_0^t \omega_+ dt' \right) \right] \quad (15b)$$

where

$$\mathcal{A}_+ = \frac{\Omega^{1/2}}{(k_y^2 c^2 + \kappa^2 + 2q\Omega ik_y c)^{1/4}} \left(\frac{2\Omega - ik_y c}{\sqrt{k_y^2 c^2 + \kappa^2}} \right) \sqrt{\frac{2\pi}{\epsilon}} e^{-\pi/4\epsilon}. \quad (16)$$

The free WKBJ solution for \hat{p}_y follows from PPV conservation,

$$\tilde{p}_y = \frac{ik_y \tilde{p}_x + 2(2-q)\Omega \tilde{\rho}}{ik_x}.$$

In the above expressions, only the value of the pseudo potential vorticity at the time of the swing (denoted by $\hat{\zeta}_s$) enters, to which the amplitude of the excited wave is directly proportional. This amplitude is exponentially small in the asymptotic limit $\epsilon \ll 1$. However, we demonstrated in paper I that our leading order asymptotic solutions are remarkably accurate even for $\epsilon \lesssim 1$, and in the case of Keplerian shear effectively hold for the entire range of azimuthal wave lengths because $\epsilon \leq 3/4$ for $0 \leq k_y H < \infty$.

4.1 Comparison of wave amplitudes

We are now in a position to test the linear theory of the excitation process by comparing the asymptotic solutions (14) and (15) with the evolution of an individual shearing wave observed in the simulation as shown in Fig. 4 and Fig. 5. For this particular wave, the azimuthal wave number $k_y = 2\pi/L_y$ and thus $\epsilon \approx 0.68$.

The result is shown in Fig. 6. As in the linear problem discussed in paper I, the numerical solution in the leading phase follows the balanced solution very closely. In the trailing phase the WKBJ solution provides an excellent match

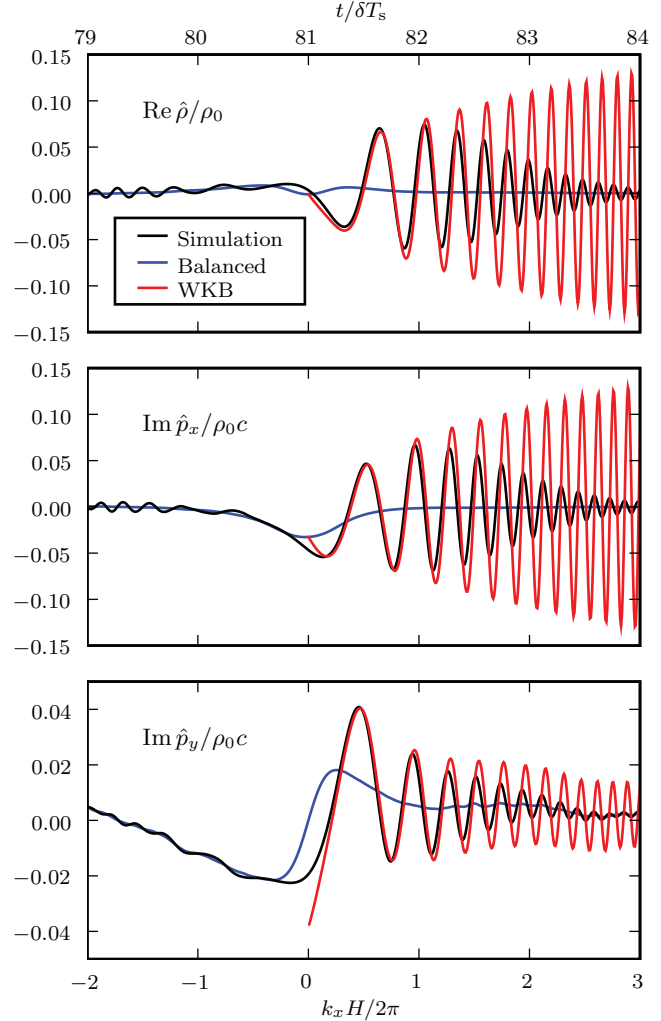


Figure 6. Comparison between simulation and linear theory for the same shearing wave as in Fig. 4. The curves shown in each panel are the wave amplitude as recorded during the simulation (black), the balanced solution (blue), and the full WKBJ solution (red). For each variable, the WKBJ amplitude in the upper panel is taken as is from linear theory and therefore grows/decays algebraically with time.

to the numerical solution for small radial wave numbers $k_x \lesssim 2\pi/H$. Roughly one shearing time after excitation, when the radial wave length is equal to the scale height H , the numerical solution starts to undergo significant damping whereas the amplitude of the WKBJ solution continues to increase algebraically. Empirically we find that the decay of the numerical solution cannot simply be attributed to viscous effects because the diffusion coefficients imposed for this simulation are at least an order of magnitude too small.

We are thus lead to believe that SD waves are damped due to nonlinear effects. It is clear that a linear shearing wave whose radial wave length decreases as its amplitude increases eventually has to break and form a shock. This phenomena has been already discussed in the context of disk physics applied to e.g. Saturn's rings (Goldreich & Tremaine 1978) and to spiral density wakes of protoplanets (Goodman

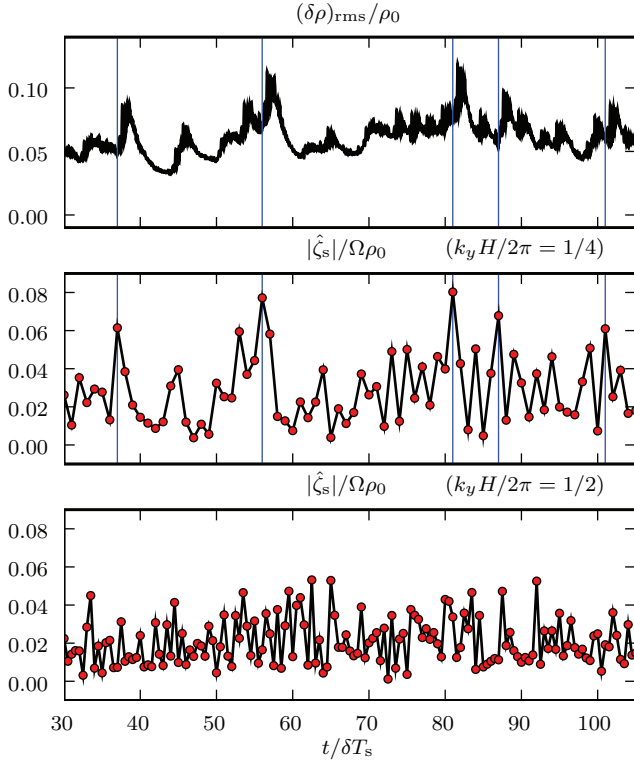


Figure 7. Upper panel: Volume averaged density fluctuations as a function of time. Here we have used high order binomial smoothing to get rid of the fast oscillations seen in Fig. 1. Lower panel: Modulus of the potential vorticity amplitude for the two smallest non-zero azimuthal wave number in the system ($k_y = 2\pi/L_y$ and $k_y = \pi/L_y$). Each red dot corresponds to an instant in time when there is a shearing wave with $k_x(t) = 0$. This happens once (twice) per shearing time for waves with $k_y = 2\pi/L_y$ ($k_y = \pi/L_y$).

& Rafikov 2001). If damping is mostly due to this effect, we conclude from Fig. 6 that shock formation must happen already when the radial wave length is roughly equal to H . This fits with the observation that SD waves usually appear as weak shocks in the simulation, see Fig. 2 and Fig. 3 as well as e.g. Gardiner & Stone (2005).

4.2 The importance of PPV

The results from the previous subsection indicate that linear theory is able to account for the initial evolution of an excited SD wave observed in the simulation. From (15) we see that the only dynamic quantity that enters the linear SD wave amplitude is the pseudo potential vorticity at the swing state, $\hat{\zeta}_s$. If the particular wave discussed in the previous subsection was not just a lucky coincidence, and linear theory holds in general as far as the initial evolution is concerned, we thus expect a correlation between $\hat{\zeta}_s$ and, for instance, the root mean squared density fluctuations,

$$(\delta\rho)_{\text{rms}} = \sqrt{\langle(\rho - \rho_0)^2\rangle_V},$$

shown in Fig. 1.

In Fig. 7 we plot $(\delta\rho)_{\text{rms}}$ as well as $|\hat{\zeta}_s|$ for the two shortest, non-zero azimuthal wave numbers available in our computational domain, denoted here by k_y^{I} and k_y^{II} , as a function

of time. The temporal correlation between $(\delta\rho)_{\text{rms}}$ and $|\hat{\zeta}_s|$ for $k_y = k_y^{\text{I}}$ is remarkably strong indeed. In particular the peak density fluctuations are seen to be delayed by roughly one shearing time with respect to the corresponding peak in $|\hat{\zeta}_s|$. This is because it takes roughly one shearing time for an SD wave to amplify to full strength after excitation, see Fig. 6. This hardly obvious correlation is perhaps the strongest evidence for the validity of our linear theory and the neglect of nonlinear source terms in the calculation of the wave amplitude.

In contrast to the above, the temporal correlation between $(\delta\rho)_{\text{rms}}$ and $|\hat{\zeta}_s|$ for $k_y = k_y^{\text{II}}$ is much weaker even though the average magnitude of $\hat{\zeta}_s$ is still roughly 70 per cent of the average magnitude for $k_y = k_y^{\text{I}}$. On one hand, this is likely to be the case because the correlation for $k_y = k_y^{\text{II}}$ is obscured and therefore harder to see, but more importantly because swing excitation – as we know from linear theory – is simply a weaker effect for $k_y = k_y^{\text{II}}$ than for $k_y = k_y^{\text{I}}$ due to the exponential dependence of the WKBJ amplitudes on k_y , see (16). We will comment on this further in the discussion section.

4.3 Angular momentum flux

In paper I we derived an expression for the radial angular momentum flux associated with a single pair of linear SD waves propagating in opposite directions,

$$\langle F_x \rangle_{yz} = -2k_y c^2 \text{Im}(\tilde{\xi}_x^* \tilde{\rho}), \quad (17)$$

see Goodman & Ryu. The angular brackets denote an average over azimuth, and as in paper I we take $k_y \geq 0$. The radial Lagrangian displacement $\hat{\xi}_x$ is defined via

$$\frac{d\hat{\xi}_x}{dt} = \frac{\hat{p}_x}{\rho_0}.$$

Note that (17) only includes the oscillatory wave part of the Fourier amplitudes, i.e. we do not account for the supposedly small contributions to the total angular momentum transport resulting from the slowly varying balanced solutions (14).

Since from a numerical point of view it is difficult to unambiguously separate the oscillatory wave part of $\hat{\xi}_x$, it is – for diagnostic purposes – more convenient to use the modified angular flux

$$\langle F'_x \rangle_{yz} = \frac{2k_y c^2}{2(2-q)\Omega\rho_0} \text{Im}(\tilde{p}_y^* \tilde{\rho}) \quad (18)$$

which does not involve the Lagrangian displacement. The two alternative expressions for the angular momentum flux, (17) and (18), are found to agree when averaged in time over one oscillation period.

It is now of interest to compare the angular momentum flux (18) associated with a single pair of SD waves observed in the simulation with linear theory by substituting the free wave solutions (15) into (18). The wave part of the Fourier amplitudes obtained from the simulations is calculated by subtracting the balanced solutions (14).

The result is shown in in Fig. 8 where we plot the modified angular momentum flux associated with the SD wave displayed in Fig. 6. As expected there is essentially no angular momentum transport prior to excitation, i.e. as long

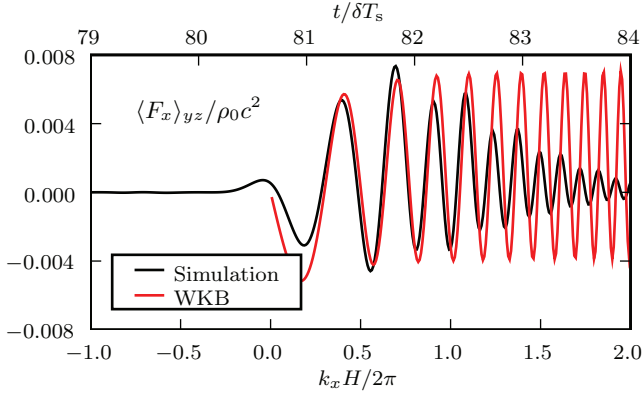


Figure 8. Angular momentum flux associated with the SD wave displayed in Fig. 6.

the waves are leading. In the trailing phase, after swing excitation has occurred, the angular momentum flux oscillates rapidly due to interference between the forward and the backward travelling wave. However, it does so around a positive mean, which means that there is net *outward* angular momentum transport.

In contrast to linear theory, the angular momentum flux observed in the simulation is strongly damped for moderately large wave numbers due to nonlinear effects. Interestingly enough, however, before the onset of damping the flux for a single pair of shearing waves observed in the simulation reaches a maximum value that is very close to what is predicted by linear theory for the far trailing regime. In spite of nonlinear damping, there will be a steady flux of angular momentum due to successive swings of shearing waves and we can thus use linear theory to make an order of magnitude estimate of the angular momentum transport due to SD waves.

In linear theory we calculated the net angular momentum flux in the far trailing regime explicitly in paper I. Averaged over one oscillation period, this flux attains a constant non-zero value given by

$$\overline{\langle F_x \rangle}_{yz} = \frac{2\pi |\hat{\zeta}_s|^2 H^2}{q\rho_0} \frac{\Omega(k_y^2 c^2 + 4\Omega^2) e^{f(\epsilon)} e^{-\pi/2\epsilon}}{[(k_y^2 c^2 + \kappa^2)^2 + (2q\Omega k_y c)^2]^{3/4}}, \quad (19)$$

as $k_x(t) \rightarrow \infty$. In the above equation,

$$f(\epsilon) = 1 - \frac{\tan^{-1}(2\epsilon)}{2\epsilon}.$$

In order to estimate the amount of angular momentum transport due to SD waves in the simulation, we thus require the swing PPV amplitude $\hat{\zeta}_s$. For shearing waves with the longest azimuthal wave length available in our computational domain, this information can be extracted from Fig. 7 where we plot the modulus of the swing PPV amplitude for all shearing waves that we observe to swing from leading to trailing. Making an ensemble average over all swings displayed in Fig. 7 we obtain

$$|\hat{\zeta}_s|^2 \approx 10^{-3} \Omega^2 \rho_0^2.$$

Substituting this into (19) yields

$$\lim_{k_x/k_y \rightarrow \infty} \overline{\langle F_x \rangle}_{yz} \approx 2.5 \cdot 10^{-4} \rho_0 c^2.$$

From this rough estimate we conclude that the mean angular momentum transport due to SD waves in the present simulation is possibly less but still significant compared to the turbulent Reynolds stress, see Fig. 1.

5 SUMMARY AND DISCUSSION

In this paper we have presented fully three-dimensional simulations of compressible MRI turbulence in which we observed the excitation of large scale, non-axisymmetric SD waves. The root mean square density fluctuations associated with these waves were shown to be correlated with the degree of turbulent activity measured by the Shakura & Syunyaev (1973) α parameter,

$$\alpha = \frac{\langle B_x B_y - \rho u_x u_y \rangle_V}{\rho_0 c^2}.$$

We performed a detailed analysis of the excitation of these waves by following the time dependent evolution of the Fourier transforms of the participating state variables. Their evolution during the excitation phase of the associated SD wave was found to be in excellent agreement with the WKB theory developed in paper I. However, shortly after the attainment of the maximum wave amplitude, the waves are rapidly damped. This damping is consistent with the sharp density profiles observed in the simulations which are indicative of the existence of shocks. Shocks are expected even under conditions of weak excitation because as shearing waves propagate their radial wavelength shortens, resulting in the onset of nonlinearity and shock formation (e.g. Goodman & Rafikov 2001). Thus the waves are always likely to be observed in the nonlinear regime. Our results indicate that for activity levels corresponding to $\alpha \sim 5 \times 10^{-3}$, being at the lower range of magnetic activities normally considered, shock formation occurs when their radial wavelength is comparable to the scale height.

The excited waves are trailing and associated with an outward angular momentum flux. The calculations performed here are consistent with the WKB theory presented in paper I in indicating that this outward flux scales in the same way as the Reynolds stress. This is supported by the fact that the density fluctuations associated with the waves are correlated with it. The level of angular momentum transport associated with SD waves is estimated to be a significant fraction of that due to the turbulent Reynolds stress $\langle -\rho u_x u_y \rangle_V$.

By consideration of the source terms for the wave excitation, we identified those associated with the pseudo potential vorticity (PPV) as the dominant ones as was assumed in paper I. Wave like structure was not seen in the PPV field, see Fig. 3, indicating that this could act consistently as an independent source generated by background turbulent fluctuations.

For the simulation discussed in detail, SD wave excitation is found to be most effective for waves with the smallest azimuthal wave number available in the computational domain. This can be understood from the theory presented in paper I. There it was found that the amplitude of an excited SD wave is directly proportional to the Fourier amplitude of the pseudo potential vorticity at the swing stage,

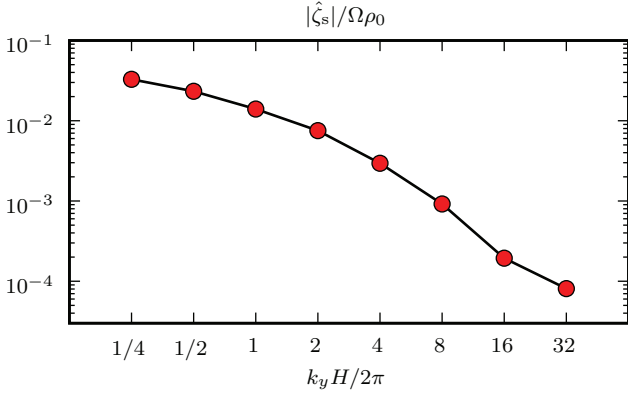


Figure 9. The spectrum of swing pseudo potential vorticity averaged over all swings as a function of azimuthal wave number k_y . The spectrum peaks at the smallest k_y , remains rather shallow at moderately small k_y , but falls off for high k_y .

$\hat{\zeta}_s$, while also having an exponential dependence on the azimuthal wave number k_y through the parameter

$$\epsilon = \frac{q\Omega k_y c}{k_y^2 c^2 + \kappa^2}.$$

If the latter dependence alone is important it implies that, for a Keplerian rotation law, SD wave production will be most effective for $k_y \sim k_y^{\text{opt}} = \Omega/c$. This is longer than the longest possible azimuthal wavelength in the shearing box considered here with $L_y = 4H$, so that SD wave production should most effective at the longest azimuthal wavelength.

The other important dependence is that of the PPV spectrum on k_y at the time of swing. This spectrum is difficult to predict theoretically, but easily determined from the simulation data. We do so by taking for each k_y an average over the ensemble of shearing waves that we find to swing from leading to trailing during the course of the simulation. The result is shown in Fig. 9. We see that the spectrum is rather shallow on large scales and falls off at small scales. A nearly flat spectrum at small k_y means that the dependence of the wave amplitude on k_y , at the most effective values, is determined by the WKBJ exponential factor appearing in e.g. (19), and should be maximal at either $k_y = 1/H$, or the smallest possible k_y in the box should that be larger. Accordingly we expect the smallest k_y to be dominant for $L_y = 4H$ but this dominance should begin to be lost once L_y starts to exceed $2\pi H$. We checked that when L_y was extended to $8H$, the contribution from the smallest k_y no longer exceeded that from the next smallest confirming the discussion given above.

Differentially rotating discs undergoing MRI driven turbulence are ubiquitous in astrophysics and the results presented here and in paper I indicate that the production of density waves is generic. The density perturbations associate with these may play an important role in driving protoplanetary migration (e.g. Nelson & Papaloizou 2004; Nelson 2005) and may play a role in exciting quasi periodic oscillations in discs around close binary stars. In the case of protoplanetary discs it has been suggested that only the high altitude regions may be turbulent while the mid-plane region lies in a ‘dead zone’ (e.g. Gammie 1996). We comment that we found that the SD waves excited by the turbulence have very weak

vertical dependence. Although we considered an unstratified disc, SD waves with weak vertical dependence also exist in the isothermal stratified case (e.g. Fromang & Papaloizou 2007), so that although they may be excited in the upper layers propagation throughout the vertical structure is to be expected with the consequence that some small but non zero transport may result throughout the disc. In this context we note that, consistently with these ideas, recent simulations by Oishi et al. (2007) that incorporated dead zones were found to have wavelike motions excited in the mid-plane regions associated with a small residual angular momentum flux that was uniformly distributed in the dead zone with a typical α value between 10^{-4} and 10^{-5} . We remark that a simple application of the WKBJ theory developed in paper I suggests, since the source of wave excitation is a vertical average of the pseudo potential vorticity, and the wave angular momentum flux is the square of this, that the value of α in the dead zone should scale as ratio of the square of the surface density in the high altitude turbulent regions to the surface density of the whole disc. However, this may be a lower bound because the dependence on surface density may actually be weaker on account of weaker dissipation in the linear regime allowing the build up of a relatively larger amount of wave angular momentum flux. This aspect remains to be investigated and decided by future much higher resolution simulations that we are unable to perform at the present time.

ACKNOWLEDGEMENTS

T. H. acknowledges support from the Science and Technology Facilities Council (STFC) as well as from the Isaac Newton Trust. The authors thank Geoffroy Lesur for fruitful discussions. Computing resources were provided by the Danish Centre for Scientific Computing (DCSC) and the University of Cambridge High Performance Computing Service.

APPENDIX A: THE PENCIL CODE

The Pencil Code (see e.g. Brandenburg & Dobler 2002) is a high-order finite-difference MHD code that is primarily designed to deal with weakly compressible turbulent flows. Solenoidality is ensured by solving the induction equation in terms of the magnetic vector potential. The equations of motion are evolved using an explicit 3rd order Runge-Kutta time stepping scheme. The scheme is stabilized by explicit diffusion coefficients.

For the purposes of the present paper, the shearing box equations that the code solved numerically consist of the continuity equation

$$\mathcal{D}\rho + \mathbf{u} \cdot \nabla \rho = -\rho \nabla \cdot \mathbf{u} + \dot{\rho}_{\text{diff}},$$

the momentum equation for an isothermal equation of state

$$\begin{aligned} \mathcal{D}\mathbf{u} + \mathbf{u} \cdot \nabla \mathbf{u} = & -2\Omega \times \mathbf{u} + q\Omega u_x \mathbf{e}_y \\ & - \frac{c^2 \nabla \rho}{\rho} + \frac{\mathbf{j} \times \mathbf{B}}{\rho} + \dot{\mathbf{u}}_{\text{diff}}, \end{aligned}$$

and the induction equation

$$\mathcal{D}\mathbf{A} = q\Omega A_y \mathbf{e}_x + \mathbf{u} \times \mathbf{B} + \dot{\mathbf{A}}_{\text{diff}},$$

where

$$\mathcal{D} = \partial_t - q\Omega x \partial_y,$$

ρ is the mass density, \mathbf{u} is the fluid velocity, \mathbf{A} is the magnetic vector potential, $\mathbf{B} = \nabla \times \mathbf{A}$ is the magnetic field, $\mathbf{j} = \nabla \nabla \cdot \mathbf{A} - \nabla^2 \mathbf{A}$ is the current density, $\boldsymbol{\Omega} = \Omega \mathbf{e}_z$ is the angular velocity, and c is the speed of sound. For Keplerian rotation $q = 3/2$.

The numerical scheme is stabilised by imposing explicit diffusion terms. For the momentum equation and the induction these take the same form as molecular diffusion, i.e.

$$\dot{\mathbf{u}}_{\text{diff}} = \nu \left(\nabla^2 \mathbf{u} + \frac{1}{3} \nabla \nabla \cdot \mathbf{u} + \frac{2\mathbf{S} \cdot \nabla \rho}{\rho} \right)$$

and

$$\dot{\mathbf{A}}_{\text{diff}} = \eta (\nabla^2 \mathbf{A} - \nabla \nabla \cdot \mathbf{A}),$$

where the traceless rate-of-strain tensor

$$S_{ij} = \frac{1}{2} \left(\frac{\partial u_i}{\partial x_j} + \frac{\partial u_j}{\partial x_i} - \frac{2}{3} \delta_{ij} \nabla \cdot \mathbf{u} \right) - \frac{q\Omega}{2} (\delta_{ix} \delta_{jy} + \delta_{iy} \delta_{jx}).$$

the values of kinematic viscosity ν and magnetic resistivity are given in the text.

In the case of the continuity equation, where there is no explicit physical diffusion coefficient, we maintain numerical stability by employing 6th order hyper diffusion, i.e.

$$\dot{\rho}_{\text{diff}} = \delta \left(\frac{\partial^6}{\partial x^6} + \frac{\partial^6}{\partial y^6} + \frac{\partial^6}{\partial z^6} \right) \rho,$$

where the mass diffusion coefficient δ is chosen to scale with the grid spacing δx ,

$$\delta \lesssim \frac{(\delta x)^5 c}{60},$$

so that significant mass diffusion only occurs near the grid scale. We note that the mass diffusion term (A) formally conserves mass and that we indeed find very little variation in the total mass during the course of the simulation.

All derivative operators are given by 6th order accurate central finite-difference formulae,

$$\begin{aligned} f'_i &= \frac{45(f_{i+1} - f_{i-1}) - 9(f_{i+2} - f_{i-2}) + (f_{i+3} - f_{i-3})}{60 \delta x} \\ f''_i &= \frac{-490f_i + 270(f_{i+1} + f_{i-1}) - 27(f_{i+2} + f_{i-2}) + 2(f_{i+3} + f_{i-3})}{180(\delta x)^2} \\ f^{(6)}_i &= \frac{20f_i - 15(f_{i+1} + f_{i-1}) + 6(f_{i+2} + f_{i-2}) - (f_{i+3} - f_{i-3})}{(\delta x)^6} \end{aligned}$$

The shearing periodic boundary condition (6a) is implemented using 6th order polynomial interpolation.

APPENDIX B: DISCRETE FOURIER TRANSFORMS IN THE SHEARING SHEET

Let us consider a prototypical evolution equation for a quantity $f(x, y, t)$ in the shearing sheet of the form

$$(\partial_t - q\Omega x \partial_y) f = c \partial_x f \quad (\text{B1})$$

We may Fourier-decompose this equation in y , but because of the explicit x -dependence we are not allowed to do so in

x . We can however transform to shearing coordinates,

$$\begin{aligned} \tilde{x} &= x \\ \tilde{y} &= y + q\Omega t x \\ \tilde{t} &= t \end{aligned}$$

so that

$$\begin{aligned} \partial_x &= \partial_{\tilde{x}} + q\Omega t \partial_{\tilde{y}} \\ \partial_y &= \partial_{\tilde{y}} \\ \partial_t &= \partial_{\tilde{t}} + q\Omega x \partial_{\tilde{y}}. \end{aligned}$$

In shearing coordinates (B1) reads

$$\partial_{\tilde{t}} \tilde{f} = c(\partial_{\tilde{x}} + q\Omega t \partial_{\tilde{y}}) \tilde{f} \quad (\text{B2})$$

where the transformed field \tilde{f} is defined through

$$\tilde{f}(\tilde{x}, \tilde{y}, \tilde{t}) = \tilde{f}(x, y + q\Omega t x, t) = f(x, y, t) \quad (\text{B3})$$

and so is obtained by shifting y by $q\Omega t x$. By transforming to shearing coordinates we have eliminated the explicit x -dependence at the expense of an explicit t -dependence on the right hand side of (B2). We now impose fully periodic boundary conditions in shearing coordinates, i.e.

$$\begin{aligned} \tilde{f}(\tilde{x} + L_x, \tilde{y}, \tilde{t}) &= \tilde{f}(\tilde{x}, \tilde{y}, \tilde{t}) \\ \tilde{f}(\tilde{x}, \tilde{y} + L_y, \tilde{t}) &= \tilde{f}(\tilde{x}, \tilde{y}, \tilde{t}). \end{aligned}$$

From (B3) it then follows that

$$f(x + L_x, y - q\Omega t L_x, t) = f(x, y, t)$$

and

$$f(x, y + L_y, t) = f(x, y, t)$$

which are just the shearing sheet boundary conditions that require periodicity in shearing coordinates

We are now in a position to Fourier decompose any field $f(x, y, t)$ in shearing coordinates,

$$\tilde{f}(\tilde{x}, \tilde{y}, \tilde{t}) = \sum_{n_x, n_y} \hat{f}_{n_x, n_y}(\tilde{t}) \exp \left[i \left(\frac{2\pi n_x}{L_x} \right) \tilde{x} + i \left(\frac{2\pi n_y}{L_y} \right) \tilde{y} \right]$$

where the Fourier coefficients can be computed from the inverse transform

$$\begin{aligned} \hat{f}_{n_x, n_y}(\tilde{t}) &= \frac{1}{L_x L_y} \iint \tilde{f}(\tilde{x}, \tilde{y}, \tilde{t}) \\ &\quad \exp \left[-i \left(\frac{2\pi n_x}{L_x} \right) \tilde{x} - i \left(\frac{2\pi n_y}{L_y} \right) \tilde{y} \right] d\tilde{x} d\tilde{y}. \end{aligned}$$

Because $d\tilde{x} d\tilde{y} = dx dy$ it follows from

$$\hat{f}_{n_x, n_y}(t) = \frac{1}{L_x L_y} \iint f(x, y, t) \exp \left[-ik_x(t)x - ik_y y \right] dx dy$$

where the wave numbers in unsheared coordinates are

$$k_x(t) = \left(\frac{2\pi n_x}{L_x} \right) + q\Omega t \left(\frac{2\pi n_y}{L_y} \right) \quad \text{and} \quad k_y = \left(\frac{2\pi n_y}{L_y} \right).$$

More explicitly

$$\begin{aligned} \hat{f}_{n_x, n_y} &= \frac{1}{L_x} \int \exp \left[-iq\Omega t \left(\frac{2\pi n_y}{L_y} \right) x \right] \\ &\quad \left\{ \frac{1}{L_y} \int f(x, y, t) \exp \left[i \left(\frac{2\pi n_y}{L_y} \right) y \right] dy \right\} \exp \left[i \left(\frac{2\pi n_x}{L_x} \right) x \right] dx \end{aligned}$$

In order to compute the Fourier transform of a real

quantity from the simulation we therefore do an FFT in y first, multiply the result with

$$\exp \left[-iq\Omega t \left(\frac{2\pi n_y}{L_y} \right) x \right], \quad (\text{B4})$$

and finally do an FFT in x . We then determine the time dependent radial wave number that each Fourier amplitude corresponds to from

$$k_x(t) = \left(\frac{2\pi n_x}{L_x} \right) + q\Omega t \left(\frac{2\pi n_y}{L_y} \right) + m \left(\frac{\pi N_x}{L_x} \right)$$

where N_x is the total number of grid points in the x -direction and the integer m is chosen such that we always have

$$-\left(\frac{\pi N_x}{L_x} \right) \leq k_x(t) \leq \left(\frac{\pi N_x}{L_x} \right).$$

Note that the phase shift (B4) corresponds to an x -dependent translation along y by an amount $-q\Omega t x$ which makes the field fully periodic in x .

REFERENCES

- Brandenburg A., Dobler W., 2002, *Computer Physics Communications*, 147, 471
 Brandenburg A., Nordlund A., Stein R. F., Torkelsson U., 1995, *ApJ*, 446, 741
 Fromang S., Papaloizou J., 2007, *A&A*, 468, 1
 Fromang S., Papaloizou J., Lesur G., Heinemann T., 2007, *A&A*, 476, 1123
 Gammie C. F., 1996, *ApJ*, 462, 725
 Gardiner T. A., Stone J. M., 2005, in de Gouveia dal Pino E. M., Lugones G., Lazarian A., eds, *Magnetic Fields in the Universe: From Laboratory and Stars to Primordial Structures*. Vol. 784 of *American Institute of Physics Conference Series*, *Energetics in MRI driven Turbulence*. pp 475–488
 Goldreich P., Tremaine S. D., 1978, *Icarus*, 34, 240
 Goodman J., Rafikov R. R., 2001, *ApJ*, 552, 793
 Hawley J. F., Gammie C. F., Balbus S. A., 1995, *ApJ*, 440, 742
 Heinemann T., Papaloizou J. C. B., 2009, *MNRAS*, in press
 Latter H. N., Lesaffre P., Balbus S. A., 2009, *MNRAS*, pp 192–+
 Nelson R. P., 2005, *A&A*, 443, 1067
 Nelson R. P., Papaloizou J. C. B., 2004, *MNRAS*, 350, 849
 Oishi J. S., Mac Low M.-M., Menou K., 2007, *ApJ*, 670, 805
 Shakura N. I., Syunyaev R. A., 1973, *A&A*, 24, 337
 Stone J. M., Hawley J. F., Gammie C. F., Balbus S. A., 1996, *ApJ*, 463, 656
 Thomson W., 1887, *Philos. Mag*, 24, 188